Title

Single-crystal based studies for correlating the properties and high-voltage performance of Li[Ni x Mn y Co 1−x−y]O 2 cathodes

Journal

Journal of Materials Chemistry A, 7(10)

ISSN

2050-7488

Authors

Zhu, Jian
Chen, Guoying

Publication Date

2019-03-05

DOI

10.1039/c8ta10329a

Peer reviewed

Journal of Materials Chemistry A

PAPER

View Article Online
View Journal | View Issue

Cite this: J. Mater. Chem. A, 2019, 7, 5463

Single-crystal based studies for correlating the properties and high-voltage performance of Li[$Ni_xMn_yCo_{1-x-y}$]O_2 cathodes†

Jian Zhu and Guoying Chen *

Received 26th October 2018
Accepted 3rd February 2019

DOI: 10.1039/c8ta10329a

rsc.li/materials-a

Safe and stable cycling of lithium-ion battery cathodes at high voltages is essential for meeting next-generation energy storage demands, yet the lack of fundamental understanding of the correlation of a material's properties and reactivities largely hinders current progress. In the present study, we show how single-crystal samples with well-controlled physical characteristics can be used to unambiguously establish the relationships among specific properties, surface chemistry and electrochemical performance, enabling rational design of better performing cathode materials. Layered Li[$Ni_xMn_yCo_{1-x-y}$]O_2 (NMC) crystals, with four different particle shapes of an octahedron (Oct), truncated octahedron (T-Oct), polyhedron (Poly) and platelet (Plate), were prepared to vary the presence of (104), (001) and (012) family facets on the surface. This represents the first experimental verification of NMC morphologies that were theoretically calculated in the past. Systematic studies on the impact of isolated physical properties reveal the important roles of the Ni content, particle size and facet on surface stability and electrochemical performance. We show that compared to (012) surface dominated samples, high-voltage cycling stability was much improved on the (001) dominated Plate sample, suggesting that replacing the (012) surface with lower energy (001) and/or (104) surfaces can be effective in stabilizing NMCs during high energy applications. Our study further provides insights into how tailoring a material's surface properties can be used as an important route in balancing cathode capacity and stability.

1. Introduction

Lithium-ion batteries (LIBs) have been the dominant power sources for portable electronics for decades and are now the mainstream energy storage choice for the electric vehicle market. With a relatively high capacity and high operating voltage, nickel-rich layered transition metal oxides with a general formula of Li[$Ni_xMn_yCo_{1-x-y}$]O_2 ($x \geq 0.5$, Ni-rich NMCs) are considered most promising for high-energy LIBs in large-scale applications.[1–6] However, the poor high-voltage cycling stability of these oxide cathodes limits their commercial adoption.[7,8] Currently, there is an urgent need for fundamental understanding of the degradation mechanism and factors that control the degradation, especially at high voltages. Such knowledge is critical in order to design future generation NMC materials with better performance and stability.[9–12]

Several processes are known to affect the stability of NMCs when cycled to high voltages, including (1) structural transformation from layered to spinel and/or rock-salt phases,[13–16] (2) mechanical damage such as crack formation in active particles,[17,18] (3) parasitic reactions between the cathode and the electrolyte,[19–21] and (4) migration, segregation and dissolution of transition metals (TMs).[22–25] Physical characteristics of primary particles, such as the composition, size and morphology, can be expected to play a large role in each of these processes. Previous studies using density functional theory (DFT) calculations revealed the importance of the primary particle surface on cathode reactivity and cycling stability.[26–29] For example, the calculation carried out on $LiCoO_2$ and NMC111 determined that their equilibrium particle shapes consist of (104), (001) and (012) facets,[26,27] and the (104) family facets are more stable than the (012) facets during electrochemical cycling. Experimentally, oxygen release and thermal decomposition of $LiCoO_2$ were found to be facet-dependent, and structural reconstruction from the layered to spinel and rock-salt phases occurred preferably on (012) and (104) family facets, as opposed to the (001) facets.[30] Ni and Co segregation was also found on selective surfaces of layered oxide cathode materials ($R\bar{3}m$ space group).[31] Recently, intra-granular cracking resulting from high-voltage cycling of layered oxides was found to progress from the grain interior along the (003) plane, which led to bulk structural degradation and reduced long-term stability.[18,32]

Energy Storage and Distributed Resources Division, Lawrence Berkeley National Laboratory, Berkeley, California 94720, USA. E-mail: gchen@lbl.gov

† Electronic supplementary information (ESI) available. See DOI: 10.1039/c8ta10329a

In conventional NMC samples, large porous aggregates of secondary particles consist of various sized primary particles. Naturally, material performance is controlled by the physical properties of primary particles as well as the properties of secondary particles, such as the particle size distribution, porosity, grain boundaries, *etc.* It is difficult to isolate the impact of a specific material's properties in these studies, which hinders systematic investigation on the influence of NMC composition, primary particle size and shape, and surface facets on their electrochemical performance and stability. Nonetheless, obtaining this understanding is essential for material design and optimization as well as correlating theoretical efforts on material behavior. Herein, we explore different approaches to synthesize NMC single-crystal samples with a variety of compositions, sizes and morphologies. For the first time, we prepare NMC single crystals with two different types of dominated surfaces, providing experimental verification for the theoretically calculated morphology. We further use this family of samples to correlate the impact of specific physical attributes on material properties and behavior. Our study provides much needed insights for rational design of layered cathode materials with improved performance and stability.

2. Experimental section

2.1. Synthesis

NMC single-crystal samples were prepared *via* a molten-salt method or co-precipitation followed by an annealing process. In a typical molten-salt synthesis, stoichiometric amounts of $Ni(NO_3)_2 \cdot 6H_2O$, $Mn(NO_3)_2 \cdot 4H_2O$ and $Co(NO_3)_2 \cdot 6H_2O$ (Sigma-Aldrich, >99%) were dissolved in a trace amount of distilled water which was then thoroughly mixed with a Li precursor (10–30 mol% in excess). The use of extra lithium precursor was necessary for compensating Li loss typically experienced during high temperature heating. A flux was then added to the mixture at a specified molar ratio between the flux and the TM precursors (denoted as *R* ratio hereafter). The mixture was further ground for 30 min, heated at 200 °C for 3 h and 850 °C for 10 h at a ramp rate of 4 °C min^{-1}, and then cooled to room temperature naturally. The final NMC products were collected by dissolving KCl in distilled water, filtering and thorough washing with distilled water. To obtain single-crystal samples with different sizes and morphologies, a combination of various TM and Li precursors, fluxes, *R* ratios and annealing conditions were used. In a typical coprecipitation–annealing method, a stoichiometric amount of metal sulfates and 0.5 g polyvinylpyrrolidone (PVP, average M_w =1 300 000 determined using the light scattering curve) were dissolved in distilled water to obtain a mixed metal sulfate solution. A NaOH/ammonia (2 M/0.2 M) aqueous solution was prepared and then added dropwise to a 1 M ammonia aqueous solution under stirring, along with the metal sulfate solution. The pH of the mixture was maintained at 11–12 for 20 h. The precipitate from the reaction was filtered and washed with distilled water several times to remove dissolved salts. The as-obtained transition metal hydroxide precursor was dried in a vacuum oven at 60 °C overnight, mixed with $LiOH \cdot H_2O$ (6 mol% excess) and annealed at 850 °C for 10 h to obtain the final NMC product.

2.2. Characterization

Powder X-ray diffraction (PXRD) was carried out using a Bruker D2 powder X-ray diffractometer (λ(Cu K_α) = 0.15418 nm, 40 kV, 30 mA). The morphology of NMC samples was characterized using a JEOL JSM-7500F field emission scanning electron microscope (SEM) at an accelerating voltage of 15 kV. The powder samples were sputtered with a thin layer of Au before the analysis to improve conduction. Chemical composition analysis was carried out using inductively coupled plasma-optical emission spectrometry (ICP-OES, Perkin-Elmer Optima 5300 DV). Hard X-ray absorption spectroscopy (hXAS) spectra of Ni, Mn and Co K-edges were collected in transmission mode using a Si (220) monochromator at Stanford Synchrotron Radiation Lightsource (SSRL) beamline 2-2. NMC powder samples were sealed between two pieces of Kapton tape for data collection. The Si (220) monochromator was re-detuned for each element before the measurement to reduce the higher harmonics in the X-ray beam. Energy calibration was carried out by setting the first inflection points in the spectra of Ni, Mn and Co metal foil references to 8333 eV, 6539 eV, and 7709 eV, respectively. X-ray absorption near edge structure (XANES) spectra were processed using SIXPACK software. Soft XAS (sXAS) spectra were collected at SSRL on the 31-pole wiggler beamline 10-1 in a single load at ambient temperature under ultra-high vacuum (10^{-9} Torr), using total electron yield (TEY) and fluorescence yield (FY) detectors. A ring current of 350 mA, a 1000 l mm^{-1} spherical grating monochromator with 40 μm entrance and exit slits, a 0.2 eV energy resolution and a 1 mm^2 beam spot were used. A thin layer of powder samples was loaded onto conductive carbon tape on an aluminum sample holder inside an argon-filled glovebox for sXAS measurement. sXAS spectral data were processed using PyMca software.

2.3. Electrochemistry

To prepare the composite electrode, the as-prepared NMC crystals, a poly(vinylidene fluoride) (PVDF) binder and an acetylene black conductive additive were mixed in *N*-methylpyrrolidone (NMP) solvent in a weight ratio of 8 : 1 : 1. The slurry was then coated onto a carbon-coated aluminum foil current collector (Exopack Advanced Coatings) and dried at 120 °C in a vacuum oven overnight. NMC composite electrodes with an area of 1.6 cm^2 and an active mass loading of ~3 mg cm^{-2} were then cut from the coated Al sheets. Half-cells were assembled in 2032-type coin cells in an argon-filled glovebox (O_2 < 1 ppm and H_2O < 1 ppm), using Li foil (Alfa-Aesar) as the counter and reference electrodes, the NMC composite electrode as the working electrode, and a Celgard 2325 membrane as the separator in a GEN 2 electrolyte (1.2 M $LiPF_6$ in ethylene carbonate (EC)/ethyl methyl carbonate (EMC), 3 : 7, Novolyte Technologies Inc.). The electrochemical performance was evaluated at ambient temperature on a VMP3 multichannel potentiostat/galvanostat controlled by EC-lab software (BioLogic Science Instruments).

3. Results and discussion

3.1. Synthesis of NMC single-crystal samples

Previously, DFT calculations reported that the equilibrium shapes of layered NMC particles are enclosed by three families of facets, namely (104), (001), and (012).[26] Among them, the surface energy of (012) and (104) is the highest and lowest, respectively, suggesting that they are the least and most thermodynamically favorable surfaces. Our recent theory-based studies showed that the surface fraction of each facet can be influenced by the chemical potentials of oxygen and lithium during synthesis. Lower oxygen chemical potential conditions, such as in a less oxidizing atmosphere or at a lower reaction temperature, favor the (104) surface over the (012) surface. On the other hand, (001) facets are more sensitive to lithium chemical potential, and their surface presence increases with decreasing lithium chemical potential. Fig. 1 depicts a schematic showing the possible equilibrium shapes of single crystal NMC enclosed by (012), (001) and/or (104). The *x*-axis shows the shape evolution as a function of O chemical potential which influences (104) presence. The *y*-axis shows the evolution as a function of Li chemical potential which influences (001) presence. Enclosed in the dashed box are possible shapes with all three families of facets. Thermodynamically, the (012)-enclosed rhombohedron has the highest surface energy and is therefore least stable under equilibrium conditions. Upon reducing O or Li chemical potential, NMC particles may evolve into a more stable morphology by diminishing the proportion of high-energy (012) facets on the surface. Experimentally, synthesis conditions that lead to the formation of particles with only one or two facet families are likely stringent or nonexistent. The possible equilibrium crystalline shapes enclosed by all three facets are shown in Fig. 1 inset, namely the (012)-dominated truncated octahedron and polyhedron, (104)-dominated tetradecahedron, and (001)-dominated platelet.

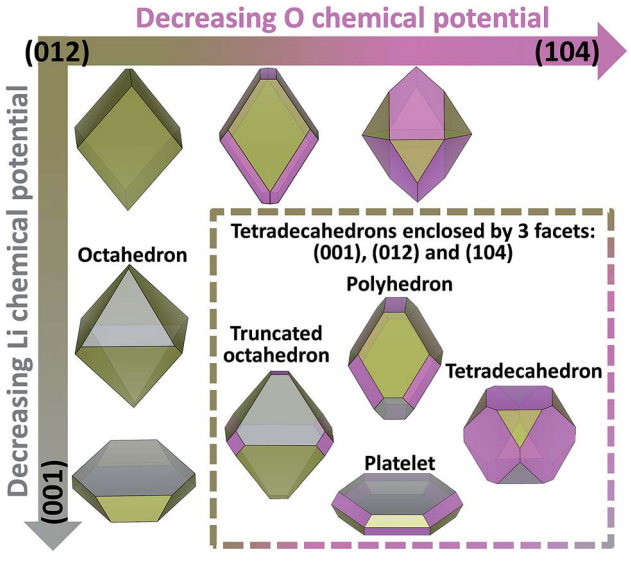

Fig. 1 Schematics showing evolution of the crystal shape as a function of O and Li chemical potentials and their influence on the presence of (012), (001) and (104) facets on the surface. The inset in the dashed line box shows various tetradecahedra enclosed by the three facets.

Based on this understanding, synthesis methods and synthesis parameters were explored to obtain NMC single crystals with various sizes and morphologies. Fig. 2 shows the SEM images of typical NMC samples prepared in this study. We obtained octahedron-shaped (Oct, Fig. 2a), truncated-octahedron-shaped (T-Oct, Fig. 2b) and polyhedron-shaped (Poly, Fig. 2c) crystal samples by using a molten-salt method where the transition-metal and Li precursors reacted at an elevated temperature in the presence of a molten flux. For the Oct sample, a mixture of CsCl and LiCl (1 : 4) was used as the flux for the reaction between the transition-metal acetates and Li_2CO_3 at 900 °C. T-Oct samples were prepared by mixing TM nitrates and lithium hydroxide or lithium carbonate in a KCl flux at an *R* ratio between 4 and 48. The typical temperature was in the range of 850 to 900 °C. To obtain the Poly samples, a mixture of TM nitrates, lithium nitrate and CsCl flux was used. The *R* ratio was reduced to 2, and the heating time was reduced to 8 h. The typical temperature used was 850 °C. Although the exact O potential for each synthesis condition is difficult to determine, the trend appears to follow the theoretical prediction that a reduction in oxygen chemical potential leads to enhanced (104) presence on the surface. For example, the Poly sample, which had the highest (104) fraction, was obtained using a lower reaction temperature and shorter reaction time. A platelet-shaped sample (Plate, Fig. 2d) was prepared *via* a coprecipitation–annealing method. The TM hydroxide precursor was first prepared in an aqueous solution containing TM sulfates, NaOH and ammonia. The as-obtained hydroxide was then mixed with LiOH and annealed at 850 or 800 °C to obtain the NMC Plate sample. Detailed synthesis conditions for obtaining each crystal sample are also summarized in Table 1. Fig. S1† shows the XRD patterns collected on the different morphologies. A hexagonal α-$NaFeO_2$ type structure with an $R\bar{3}m$ space group was confirmed for all samples. Analysis of XRD peak intensity confirms the nature of anisotropic crystal growth. For example, the (012)/(003) and (104)/(003) intensity ratios of the Plate sample are 0.17 and 0.75, respectively, while they are around 0.1 and 0.4–0.5 for Oct, T-Oct, and Poly samples. The larger ratios of the Plate sample are consistent with the preferred growth direction along ⟨012⟩ and ⟨104⟩ relative to ⟨003⟩, which results in a (001)-dominated surface. The similarity in the XRD patterns of Oct, T-Oct, and Poly samples is likely due to the presence of the same (012)-dominated surface for all three samples.

The single-crystal nature of NMC samples prepared using the same procedure was investigated in a previous publication.[33] Particles were surveyed by SAED to verify the single crystalline orientation throughout the particle. In this study, shape analysis was used to index the planes and also quantify their relative percentage on the surface. Based on the SEM image shown in Fig. 2, crystal shapes of each sample were built and analyzed by using VESTA (JP-Minerals), a 3D visualization program for structural models. While the surfaces of Oct, T-Oct and Poly samples were dominated by (012) facets, the presence of (104) facets gradually increased with the increase of truncation. More

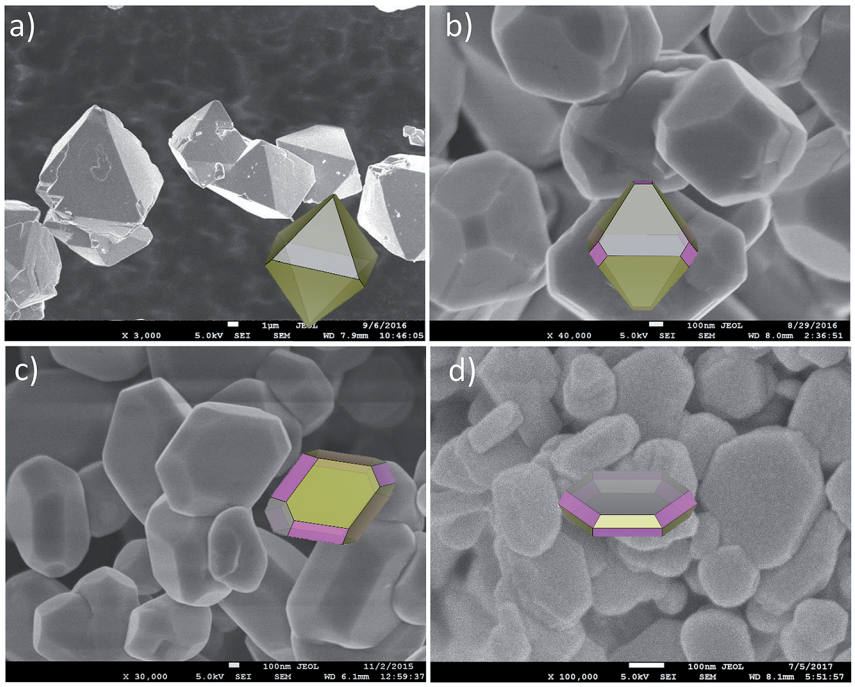

Fig. 2 SEM images of NMC crystal samples with four different morphologies: (a) octahedron-shaped (Oct), (b) truncated-octahedron-shaped (T-Oct), (c) polyhedron-shaped (Poly) and (d) platelet-shaped (Plate).

specifically, while the Oct crystals were enclosed by 88% of (012) facets and 12% percent of (001), T-Oct crystals had 85% of (012), 10% of (001) and 5% of (104) facets. For the Poly sample, the percentage changed to 70%, 5% and 25% for (012), (001) and (104), respectively. The most significant difference between the Plate and the Oct/T-Oct/Poly sample series lies in the ratio between (001) and (012) facets as more than 85% of the Plate surface is covered by the (001) facets (Fig. 3).

NMC single-crystal samples with the size ranging from 10 μm to 0.1 μm were also prepared. For simplicity, only the synthesis of T-Oct NMC532 is discussed here, although other compositions were also made under similar conditions. We found that the size of T-Oct shaped single crystals is most sensitive to the type and amount of the flux as well as the annealing conditions used during the synthesis. In general, the crystal size decreases with the increasing R ratio between the flux and the TM precursors. Particles larger than 0.5 μm were obtained by using a small amount of CsCl or KCl flux ($R \leq 4$), whereas those below 0.5 μm can be prepared by using a large amount of KCl flux ($R = 48$). Fig. 4 shows the SEM images of the obtained T-Oct NMC532 crystals with various particle sizes.

The above synthesis approaches are mostly applicable for preparing NMC crystal samples with different compositions and a series of morphology- and size-controlled NMC333, NMC532, NMC622 and NMC811 were synthesized. The chemical compositions of the samples were analyzed and verified by

Table 1 Synthesis conditions for NMC crystal samples

NMC samples						
Composition	Morphology	Size (μm)	Precursors	Flux/R ratio	T (°C)	t (h)
333 or 622	Oct	10	TM acetates/Li_2CO_3	CsCl/LiCl = 1/4	900	12
532	T-Oct	10	TM acetates/Li_2CO_3	CsCl/4	850	12
811	T-Oct	10	TM nitrates/LiOH	CsCl/4	900	12
333 or 622	T-Oct	1	TM nitrates/LiOH	CsCl/4	900	12
532	T-Oct	1	TM nitrates/ Li_2CO_3	CsCl/4	900	12
811	T-Oct	1	TM nitrates/LiOH	KCl/4	850	10
532	Poly	1	TM nitrates/ $LiNO_3$	CsCl/2	850	8
333 or 532	T-Oct	0.5	TM nitrates/ $LiNO_3$	KCl/4	850	12
333, 532 or 622	T-Oct	0.1	TM nitrates/LiOH	KCl/48	850	12
811	T-Oct	0.1	TM nitrates/LiOH	KCl/48	880	10
333	Plate	0.1	TM hydroxides/LiOH	—	850	10
622	Plate	0.1	TM hydroxides/LiOH	—	800	10

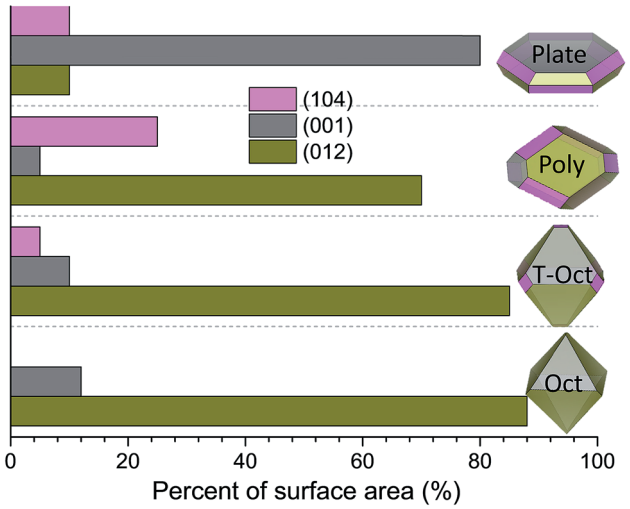

Fig. 3 Percentage of each family of crystal facets appearing on the surface of the synthesized NMC crystal samples.

ICP analysis, and the results are summarized in Table S1.† The large library of samples allowed us to investigate the role of specific oxide properties while maintaining all others the same within the series. In the following sections, we discuss in detail the impact of Ni content, particle size and surface facets on the NMC structure, chemical properties, and cathode performance and stability.

3.2. Impact of the NMC Ni content

To investigate the role of Ni content, we focused on a series of NMC crystal samples with three different compositions of 333, 622 and 811, all with the same size of 1 μm, the same shape of the truncated octahedron and (012)-dominated surface, and the same Mn/Co ratio. Fig. 5a shows the XRD patterns of the samples, with the inset showing the atomic structure of layered NMC. In the typical hexagonal α-$NaFeO_2$ type structure with an $R\bar{3}m$ space group, lithium cations occupy the octahedral 3b sites and TM (Ni, Mn and Co in this case) cations co-occupy the

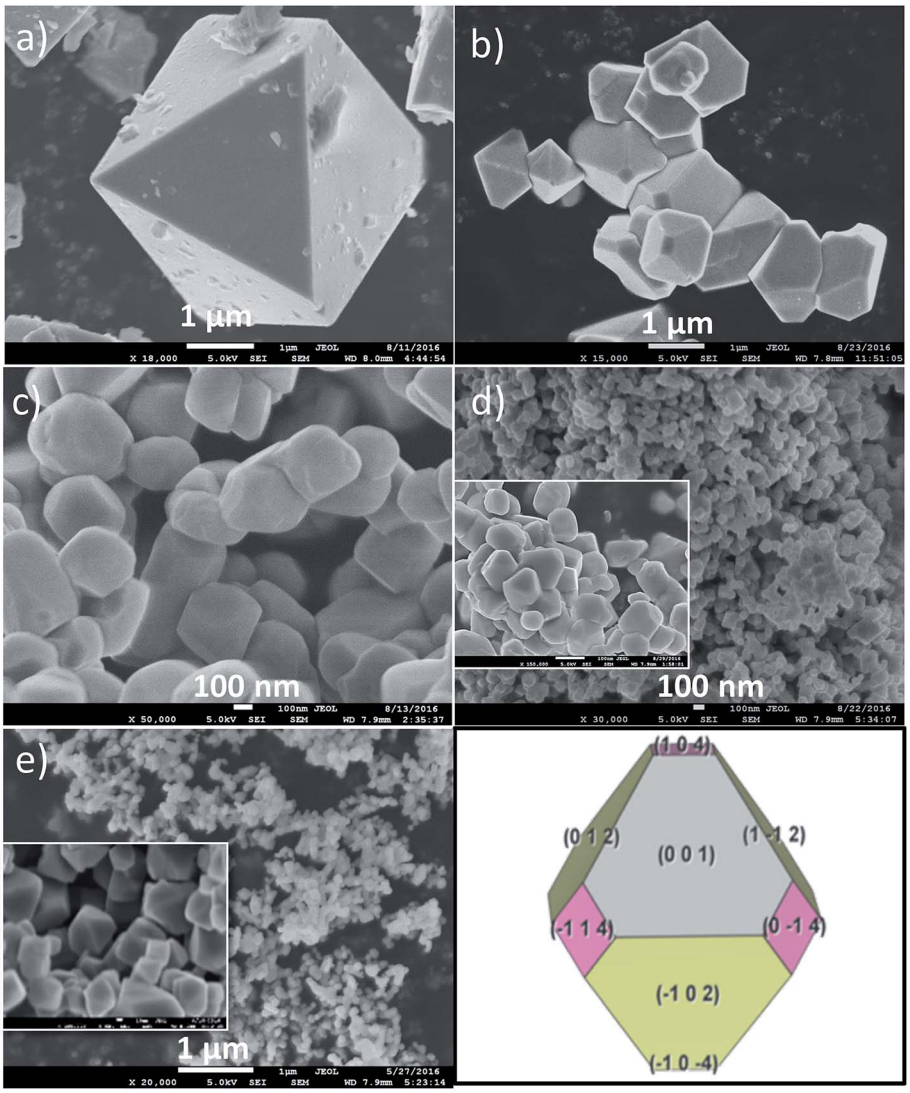

Fig. 4 SEM images of T-Oct NMC532 with different sizes: (a) 10 μm, (b) 1 μm, (c) 0.5 μm, (d) 0.1 μm, and (e) 50 nm. (f) Facet index on the T-Oct surface.

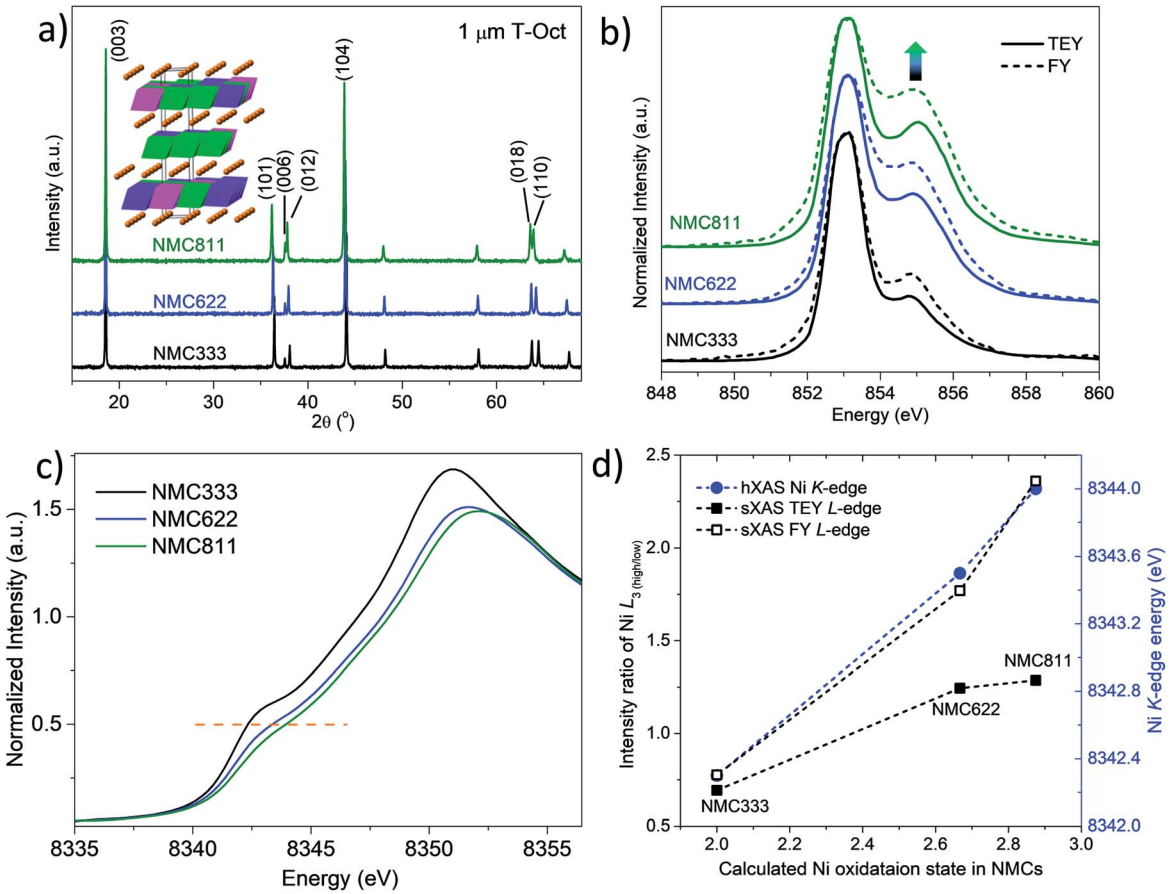

Fig. 5 a) XRD patterns, (b) Ni L_3-edge soft XAS spectra collected in TEY and FY modes, (c) Ni K-edge hard XAS spectra, and (d) changes in the ratio of high energy/low energy L_3-edge peaks and K-edge energy positions as a function of the calculated Ni oxidation state of 1 μm T-Oct NMC333, NMC622 and NMC811 samples.

octahedral 3a sites to form the transition-metal layer. Peak splitting in (006)/(012) and (018)/(110) doublets is typically observed,[34] which is often used as an indicator for structural ordering in the hexagonal crystal structure. The presence of peak splitting in the XRD patterns collected on all three samples confirms the formation of the layered structure. With the increase of Ni content, the splitting gradually narrowed, which suggests a reduction in the layering quality. This is consistent with the increasing cation mixing resulting from the size similarity between Ni^{2+} (0.69 Å) and Li^{+} (0.76 Å), as reported in previous studies.[35] The enhanced cation mixing in NMC811 is also evidenced by the decreased intensity ratio of $I(003)/I(104)$ in the XRD pattern.

Rietveld refinement of the XRD patterns collected on NMC333, NMC622 and NMC811 T-Oct samples was carried out, and the results are shown in Fig. S2.† The a and c lattice parameters for NMC333, NMC622 and NMC811 were 2.8646(1) and 14.2336(1) Å, 2.8752(1) and 14.2339(4) Å, and 2.8883(4) and 14.251(2) Å, respectively. These values are similar to what was reported in the literature.[12,36–41] With increasing Ni content, the smaller Co^{3+} (0.545 Å) and Mn^{4+} (0.53 Å) are replaced by larger-sized Ni cations, either Ni^{2+} (0.69 Å) or Ni^{3+} (0.60 Å), which leads to an overall increase in the lattice dimension. The c/a ratio, on the other hand, decreased from 4.97 in NMC333 to 4.93 in NMC811, further confirming reduced quality in the layered structure due to increased Ni/Li cation mixing.

Synchrotron soft XAS with depth profiling capability was used to probe the chemical changes on the surface and in the surface-bulk region. By using TEY and FY detectors, TM oxidation states on the top 5 and 50 nm can be evaluated, respectively. Fig. 5b shows the Ni L_3-edge spectra collected on NMC333, NMC622 and NMC 811 T-Oct samples. As the intensity ratio between the high energy and low energy L_3 peaks (I_{high}/I_{low}) is often used as an index for the Ni oxidation state,[42–45] we normalized all the spectra to the intensity of the low energy peak. With increasing Ni content, an increase in the intensity of the high energy L_3 peak was observed in both TEY and FY spectra, consistent with the increase of Ni oxidation state in higher Ni content NMCs. The stronger high energy peak in FY mode as compared to that in the TEY mode indicates that surface Ni is at a lower oxidation state, likely a result of surface reduction as observed in previous studies.[43,44] The oxidation state of Mn and Co, however, was not influenced by the Ni content as the L_3-edge sXAS spectra of Mn and Co are nearly identical for all three samples (Fig. S3a and S3b†). Based on the TM reference spectra (Fig. S4†), Mn and Co oxidation states were determined to be 4+ and 3+, respectively. The oxidation state of bulk TMs was evaluated by hard XAS, and the results for

Ni, Mn and Co are shown in Fig. 5c, S3c and S3d†, respectively. With increasing Ni content, Ni K-edge energy, determined using the intensity at 0.5 in the normalized spectrum, gradually shifted towards a higher value, consistent with an increase in the bulk oxidation state. The Mn and Co K-edge spectra in Fig. S3c and S3d† further confirm that bulk Mn and Co are in 4+ and 3+ states, respectively, and their oxidation states are independent of the Ni content in the NMC.

Fig. 5d compares the Ni K-edge energy position as well as the intensity ratios of high energy/low energy L_3 peaks as a function of theoretical Ni oxidation state in the NMC. A similar linear relationship was observed for the K-edge energy and FY L-edge intensity ratio, corresponding to the increase of Ni oxidation state from +2 in NMC333 to +2.88 in NMC811 in both bulk and surface-bulk regions. The TEY intensity ratio is generally lower, and the difference becomes more significant as the Ni content increases, a result of higher surface reactivity in the presence of Ni^{3+}.

Fig. 6 compares the electrochemical performance of the crystals. The samples were made into composite electrodes and cycled in a half cell at a constant rate of C/10 between 3–4.3 V and 3–4.6 V. Because the Ni redox reaction occurs at lower potential than that of Co, increasing the Ni content in NMC leads to more Li extraction and an increase in the initial discharge capacity in both voltage windows. As expected, initial capacity also increases with increasing upper cutoff voltage from 4.3 to 4.6 V. In both cases, there is an increase in the rate of capacity fade, as shown in the capacity retention plot in Fig. 6b. The study demonstrates the intrinsic trade-offs between capacity and the electrochemical stability, in the absence of the influence of particle microstructure such as the size, morphology and porosity.

3.3. Impact of the NMC primary particle size

Fig. 7a shows the XRD patterns collected on three NMC532 crystal samples with a particle size of 10 μm, 1 μm and 0.1 μm, respectively, all with the same T-Oct shape and (012)-dominated surface. The samples had a well-ordered layered structure with the splitting in (006)/(012) and (018)/(110) doublet peaks clearly shown. Results from the Rietveld refinements (Fig. S5†) showed that *a* and *c* lattice parameters for the 10, 1 and 0.1 μm NMC532 samples were 2.8671(5) and 14.2374(6) Å, 2.8771(1) and 14.2587(8) Å, and 2.8765(1) and 14.2578(8) Å, respectively. While the values for the 1 and 0.1 μm samples are consistent with those reported in the literature,[36–41] the slightly reduced lattice dimension in the 10 μm sample may suggest mechanical strain in the much larger NMC particles. The similarity in the *c*/*a* ratio in 0.1 and 1 μm samples further suggests that synthesis parameters are not likely to play a significant role in the layered structure.

Fig. 7b shows Ni, Mn and Co TEY L_3-edge soft XAS profiles collected on the three samples. In NMC532, the theoretical oxidation states of Ni, Mn and Co are 2.4+, 4+ and 3+, respectively. When the particle size reduced from 10 to 1 μm, there is a reduction in the intensity ratio between the high energy peak and the low energy peak in the L_3 profile, suggesting a lower Ni oxidation state. The ratio in the 1 and 0.1 μm samples, on the other hand, are similar. This is likely a result of the increased surface area for smaller particles where more Ni reduction can occur. Compared to the standard spectra shown in Fig. S4,† the Mn and Co L-edge spectra of all three samples suggest that their respective oxidation states are close to the theoretical values of 4+ and 3+. The bulk oxidation states of the TMs were also evaluated by hard XAS and K-edge XANES, and the spectra are shown in Fig. 7c. These results are consistent with the oxidation states of 2.4+, 4+ and 3+ for Ni, Mn and Co, confirming the similar bulk chemical properties of the samples.

We further evaluated the electrochemical performance of the samples through galvanostatic cycling (Fig. 8a and b) and rate capability testing (Fig. 8c). The crystals were prepared into composite electrodes and cycled in a half cell at a constant rate of C/10 between 3–4.3 V and 3–4.6 V. As shown in Fig. 8a, decreasing the particle size increases the initial discharge capacity in both voltage windows. When cycled to the upper cutoff voltage of 4.3 V, the 1st cycle discharge capacities were 116, 127 and 132 mA hg^{-1} for 10, 1 and 0.1 μm samples, respectively. The lower capacity for the 10 μm sample is likely a result of kinetic hindrance and poorer material utilization. As expected, increasing the upper cutoff voltage to 4.6 V increases the initial discharge capacity but at the expense of cycling stability. The 1st cycle discharge capacities were 188, 183 and 191 mA h g^{-1} for 10, 1 and 0.1 μm samples, respectively. These similar values suggest that the over-potential at the higher

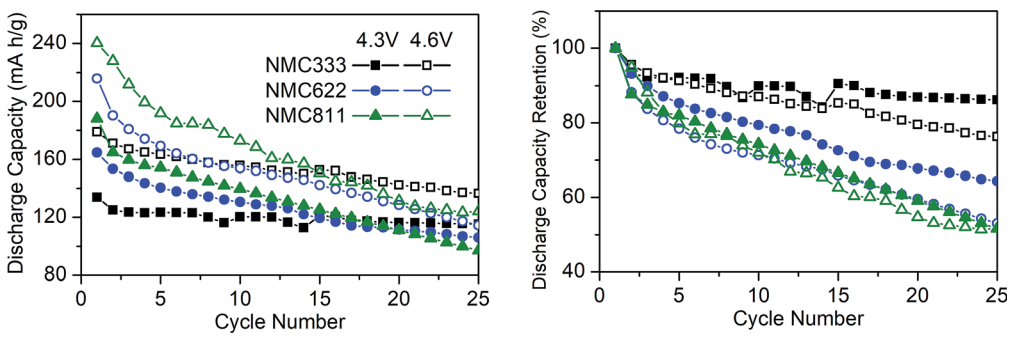

Fig. 6 The impact of the Ni content on the electrochemical performance of 1 μm sized T-Oct NMC333, NMC622 and NMC811: (a) discharge capacity as a function of cycle number and (b) discharge capacity retention.

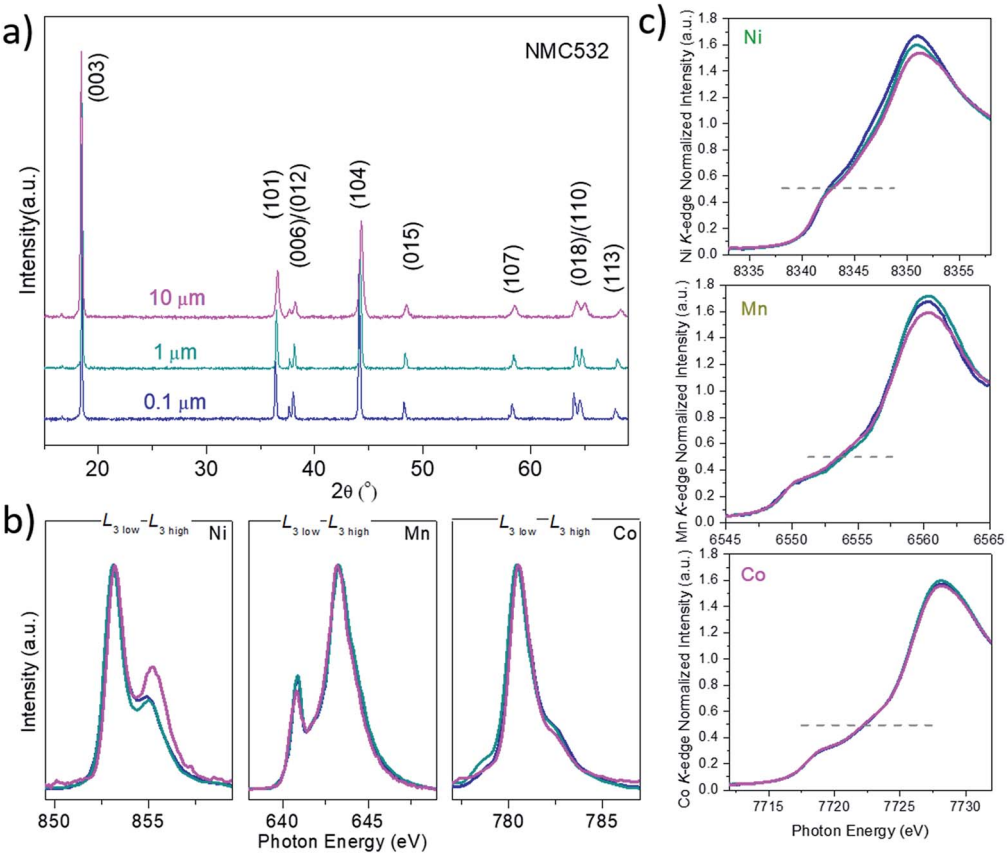

Fig. 7 a) XRD patterns, (b) Ni, Mn and Co soft XAS L_3-edge spectra in TEY mode, and (c) K-edge XANES spectra of pristine NMC532 T-Oct with a particle size of 10 μm, 1 μm and 0.1 μm.

voltage is able to extract more Li and greatly improve the utilization of the large particles. Fig. 8b directly compares the particle size effect on the cycling stability in both voltage windows. When cycled between 3 and 4.3 V, the 10 μm sample only slightly outperforms 1 and 0.1 μm samples, which exhibited similar performances. With the higher cutoff voltage of 4.6 V, there is an overall decrease in cycling stability as charge/discharge with a larger extent of Li involvement naturally destabilized the layered crystal structure. Liquid electrolytes are typically reactive above 4.3 V, and side reactions between the cathode and the electrolyte further contribute to the instability. The smaller particles had a larger surface-to-volume ratio and therefore experienced more severe deterioration due to the side reactions, as compared to the 10 μm sample. We further compare the performance of the samples at C/25, C/10 and C/5 rates, and the results are shown in Fig. 8c. At all cycling rates, the 10 and 0.1 μm samples had the lowest and highest discharge capacity, respectively. This is consistent with the observation that larger particles have poorer material utilization due to the longer Li diffusion length.[46]

3.4. Impact of the NMC surface facet

To evaluate the impact of surface facets, comparative studies were performed on (001) surface-dominated Plate and (012) surface-dominated T-Oct NMC333 samples, both with the same size of 0.1 μm. Fig. 9a shows the XRD patterns collected on the samples. The layered crystal structure was obtained, with the clear splitting in (006)/(012) and (018)/(110) peaks confirming a low degree of cation mixing in NMC333. Although the structural index in the XRD is the same, the orientation effect is obvious when the peak intensity ratio is analyzed. Smaller (003)/(012) and (003)/(104) peak intensity ratios were observed for the Plate sample, consistent with the slower growth along the ⟨003⟩ direction and a larger presence of (001) on the surface, as compared to that of the (012) surface-dominated T-Oct sample.

Comparison of the TEY and FY Ni L-edge soft XAS profiles is shown in Fig. 9b. The Plate sample experienced less surface Ni reduction than the T-Oct sample, as indicated by the higher intensity ratio between the high energy and low energy peaks. This suggests that the (001) surface with lower surface energy is more resistant to chemical reduction during synthesis and processing. Bulk Ni remains in the 2+ state in both samples, as shown in Ni K-edge hard XAS profiles in Fig. 9c. The presence of Mn^{4+} and Co^{3+} in the bulk is also confirmed by Mn and Co K-edge hXAS profiles in Fig. S6.†

Fig. 10 compares the cycling performance of the NMC333 samples. When cycled to the upper cutoff voltage of 4.3 V, the initial discharge capacities of the T-Oct and Plate samples were similar at about 125 mA h g^{-1}. Increasing the cutoff voltage to 4.6 V leads to an increase in discharge capacity, but the change

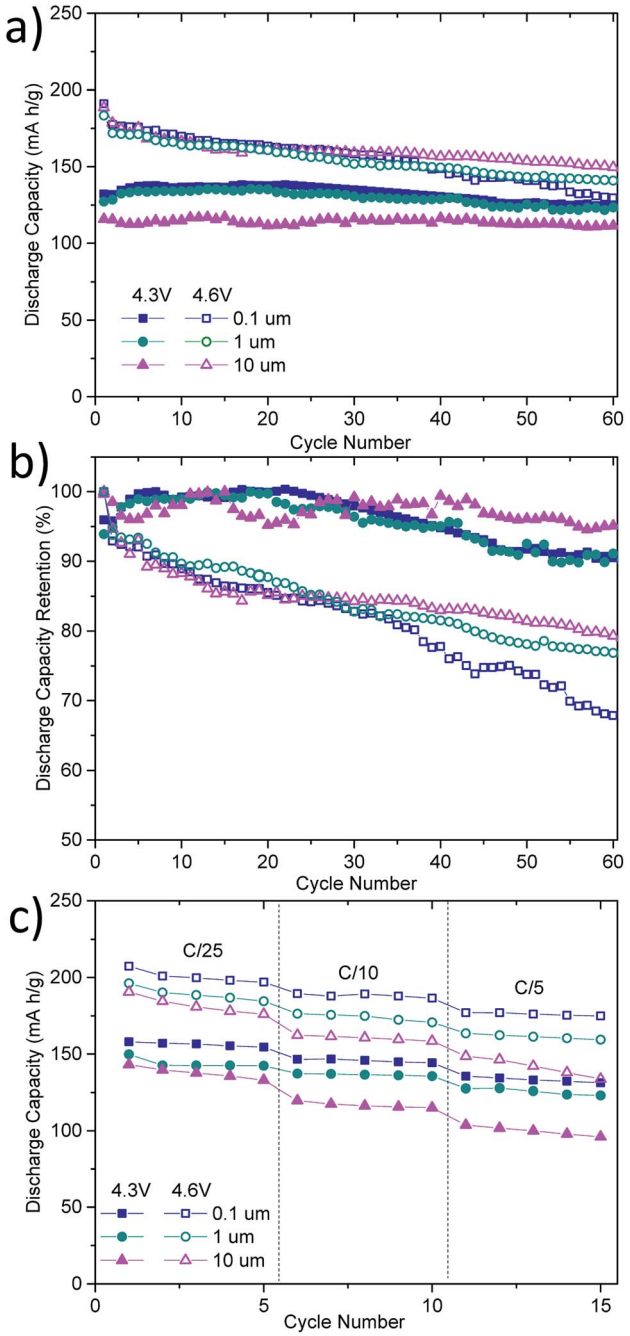

Fig. 8 a) Discharge capacity, (b) capacity retention at C/10 and (c) rate capability of NMC532 crystal samples cycled between 3.0–4.3 V (solid) and 3.0–4.6 V (hollow), respectively.

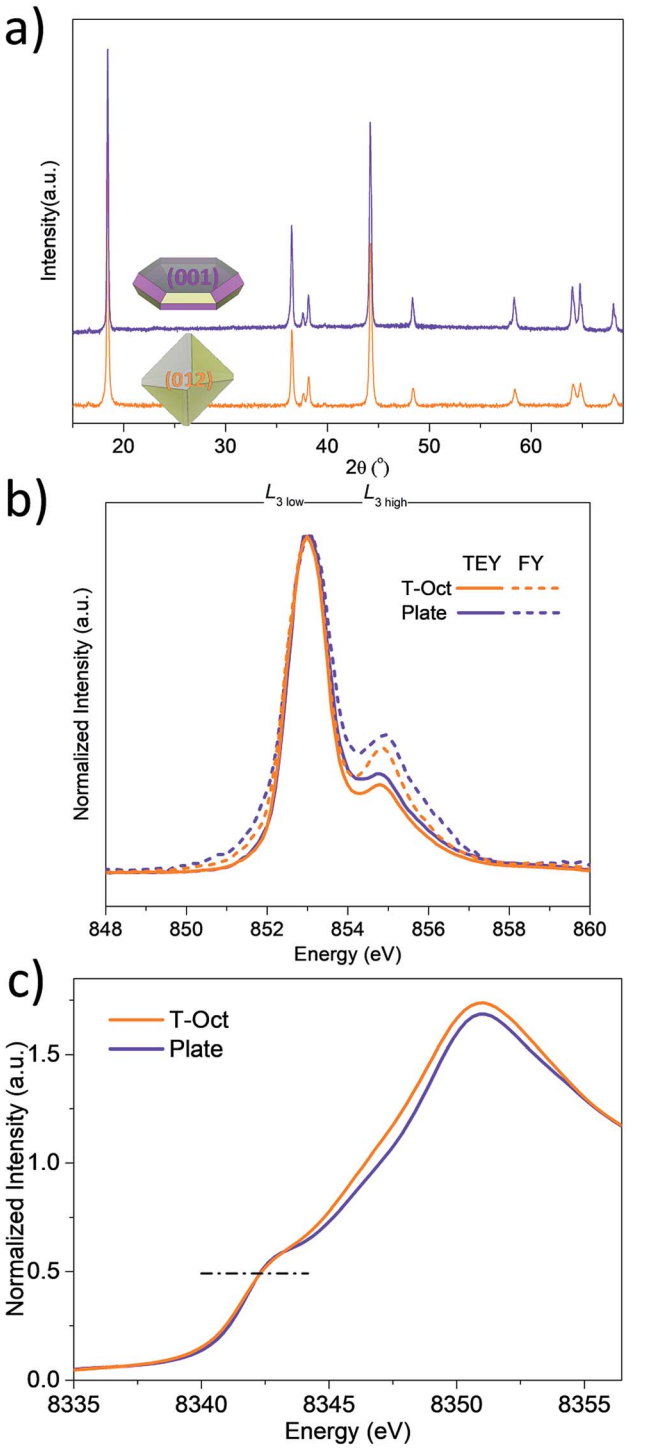

Fig. 9 a) XRD patterns, (b) sXAS Ni L_3-edge spectra in TEY and FY modes and (c) hXAS Ni K-edge spectra of 0.1 μm NMC333 samples, with T-Oct dominated by (012) and Plate dominated by (001).

is more significant for the T-Oct sample which delivered 171 mA h g^{-1}, whereas the Plate sample had 157 mA h g^{-1}. This difference is likely due to enhanced material utilization driven by the over-potential. NMC333 with the (012)-dominated surface benefited more from the driving force than that with the (001) surface, which is impermeable to Li. The increase in initial discharge capacity, however, comes at the expense of the cycling stability, as faster capacity decay is clearly shown in Fig. 10b. The results clearly show that surface facets have a significant impact on electrochemical performance at both low and high cutoff voltages. As the (001) surface is parallel to the TM layers, it is impermeable to Li.[26,27] On the other hand, the (012) surface has efficient Li diffusion pathways. The net result is that particles with a large (001) surface tend to have lower utilization and capacity but better stability as compared to the sample with the (012) surface. The higher surface energy of (012) family facets

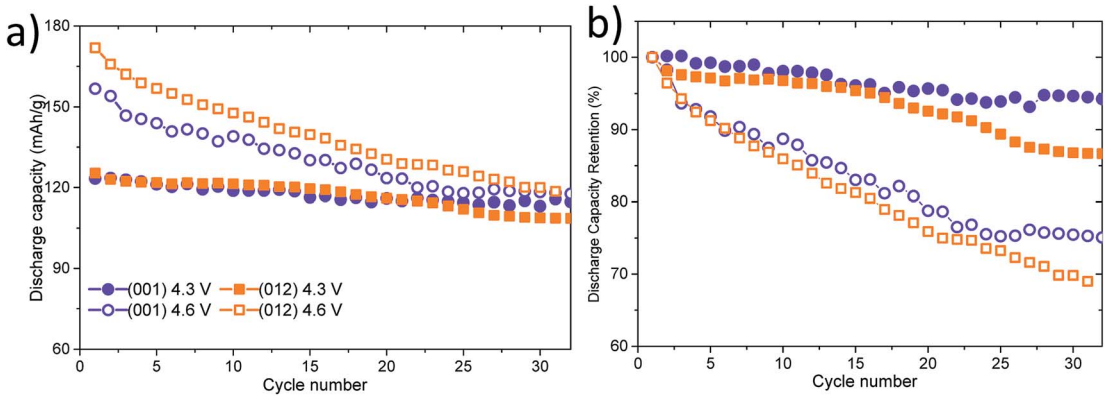

Fig. 10 a) Cycling stability at C/10 and (b) discharge capacity retention when cycled between 3.0–4.3 V (solid) and 3.0–4.6 V (hollow).

also makes them more reactive and less stable during electrochemical cycling.

4. Conclusions

By using different synthesis approaches and synthesis conditions, a large library of layered NMC single-crystal samples with various chemical compositions of 333, 532, 622, and 811, various sizes ranging from 0.1 to 10 μm, and various morphologies of Oct, T-Oct, Poly and Plate was synthesized. This allows the investigation of the role of specific NMC properties, such as the Ni content, size and surface facet, well isolated from the interference from each other as well as other uncontrolled factors. We found that increasing the Ni content leads to a lower quality layered structure, more severe surface Ni reduction, and higher initial capacity but poorer cycling stability. Smaller primary particles experienced enhanced surface TM reduction, a direct result of the increased ratio between the surface area and volume. Furthermore, when the particle size was reduced, a better rate performance was achieved because of the shorter Li diffusion length. Surface facets were found to play a critical role in material stability and cycling performance. The (012) surface is generally more reactive than that of (001), which is evidenced by enhanced surface Ni reduction and higher initial discharge capacity but poorer cycling stability of the T-Oct samples, as compared to the Plate sample. For high energy applications that require stable operation at high voltages, replacing the more reactive (012) surface with a less reactive (001) or (104) surface is an effective strategy. This can be achieved by adjusting synthesis conditions that favor particles with (001) and/or (104) surfaces over the (012) surface. Although the tradeoff between cathode capacity and stability remains a challenge, our study demonstrates that surface engineering provides an additional avenue in material optimization.

Conflicts of interest

There are no conflicts to declare.

Acknowledgements

We thank Dr Jianhua Yan and Dr Wang Hay Kan for experimental assistance, Dr Hakim Iddir, Dr Jason Croy and Dr Juan Garcia at Argonne National Laboratory for fruitful discussions, and Dr Marca Doeff, Dr Dennis Nordlund and Dr Ryan Davis for the help with the XAS measurements carried out at SSRL. Use of the Stanford Synchrotron Radiation Lightsource, SLAC National Accelerator Laboratory, was supported by the U.S. Department of Energy, Office of Science, Office of Basic Energy Sciences under Contract No. DE-AC02-76SF00515. This work was supported by the Assistant Secretary for Energy Efficiency and Renewable Energy, Office of Freedom CAR and Vehicle Technologies of the U.S. Department of Energy under Contract No. DE-AC02-05CH11231.

References

1 Y. Ding, D. Mu, B. Wu, R. Wang, Z. Zhao and F. Wu, Recent progresses on nickel-rich layered oxide positive electrode materials used in lithium-ion batteries for electric vehicles, *Appl. Energy*, 2017, **195**, 586–599.

2 J. Xu, F. Lin, M. M. Doeff and W. Tong, A review of Ni-based layered oxides for rechargeable Li-ion batteries, *J. Mater. Chem. A*, 2017, **5**(3), 874–901.

3 C. S. Yoon, M. H. Choi, B. B. Lim, E. J. Lee and Y. K. Sun, Review-High-Capacity Li $Ni_{1-x}Co_x/2Mn_x/2O_2$ (x = 0.1, 0.05, 0) Cathodes for Next-Generation Li-Ion Battery, *J. Electrochem. Soc.*, 2015, **162**(14), A2483–A2489.

4 F. Schipper, E. M. Erickson, C. Erk, J.-Y. Shin, F. F. Chesneau and D. Aurbach, Review—Recent Advances and Remaining Challenges for Lithium Ion Battery Cathodes: I. Nickel-Rich, $LiNi_xCo_yMn_zO_2$, *J. Electrochem. Soc.*, 2017, **164**(1), A6220–A6228.

5 A. Konarov, S. T. Myung and Y. K. Sun, Cathode Materials for Future Electric Vehicles and Energy Storage Systems, *ACS Energy Lett.*, 2017, **2**(3), 703–708.

6 W. Liu, P. Oh, X. Liu, M. J. Lee, W. Cho, S. Chae, Y. Kim and J. Cho, Nickel-Rich Layered Lithium Transition-Metal Oxide for High-Energy Lithium-Ion Batteries, *Angew. Chem., Int. Ed.*, 2015, **54**(15), 4440–4457.

7 J. Li, J. Camardese, R. Shunmugasundaram, S. Glazier, Z. Lu and J. R. Dahn, Synthesis and Characterization of the Lithium-Rich Core–Shell Cathodes with Low Irreversible Capacity and Mitigated Voltage Fade, *Chem. Mater.*, 2015, **27**(9), 3366–3377.

8 W. Li, B. Song and A. Manthiram, High-voltage positive electrode materials for lithium-ion batteries, *Chem. Soc. Rev.*, 2017, **46**(10), 3006–3059.

9 E. Hu, X. Wang, X. Yu and X.-Q. Yang, Probing the Complexities of Structural Changes in Layered Oxide Cathode Materials for Li-Ion Batteries during Fast Charge–Discharge Cycling and Heating, *Acc. Chem. Res.*, 2018, **51**(2), 290–298.

10 C. Tian, F. Lin and M. M. Doeff, Electrochemical Characteristics of Layered Transition Metal Oxide Cathode Materials for Lithium Ion Batteries: Surface, Bulk Behavior, and Thermal Properties, *Acc. Chem. Res.*, 2017, **51**(1), 89–96.

11 F. Lin, Y. Liu, X. Yu, L. Cheng, A. Singer, O. G. Shpyrko, H. L. Xin, N. Tamura, C. Tian, T.-C. Weng, X.-Q. Yang, Y. S. Meng, D. Nordlund, W. Yang and M. M. Doeff, Synchrotron X-ray Analytical Techniques for Studying Materials Electrochemistry in Rechargeable Batteries, *Chem. Rev.*, 2017, **117**(21), 13123–13186.

12 H.-H. Sun and A. Manthiram, Impact of Microcrack Generation and Surface Degradation on a Nickel-Rich Layered $Li[Ni_{0.9}Co_{0.05}Mn_{0.05}]O_2$ Cathode for Lithium-Ion Batteries, *Chem. Mater.*, 2017, **29**(19), 8486–8493.

13 A. Manthiram, B. Song and W. Li, A perspective on nickel-rich layered oxide cathodes for lithium-ion batteries, *Energy Storage Materials*, 2017, **6**, 125–139.

14 S.-K. Jung, H. Gwon, J. Hong, K.-Y. Park, D.-H. Seo, H. Kim, J. Hyun, W. Yang and K. Kang, Understanding the Degradation Mechanisms of $LiNi_{0.5}Co_{0.2}Mn_{0.3}O_2$ Cathode Material in Lithium Ion Batteries, *Adv. Energy Mater.*, 2014, **4**(1), 1300787.

15 L. Zou, W. Zhao, Z. Liu, H. Jia, J. Zheng, G. Wang, Y. Yang, J.-G. Zhang and C. Wang, Revealing Cycling Rate-Dependent Structure Evolution in Ni-Rich Layered Cathode Materials, *ACS Energy Lett.*, 2018, **3**(10), 2433–2440.

16 F. Lin, I. M. Markus, D. Nordlund, T.-C. Weng, M. D. Asta, H. L. Xin and M. M. Doeff, Surface reconstruction and chemical evolution of stoichiometric layered cathode materials for lithium-ion batteries, *Nat. Commun.*, 2014, **5**, 3529.

17 H.-H. Ryu, K.-J. Park, C. S. Yoon and Y.-K. Sun, Capacity Fading of Ni-Rich $Li[Ni_xCo_yMn_{1-x-y}]O_2$ ($0.6 \leq x \leq 0.95$) Cathodes for High-Energy-Density Lithium-Ion Batteries: Bulk or Surface Degradation?, *Chem. Mater.*, 2018, **30**(3), 1155–1163.

18 P. F. Yan, J. M. Zheng, M. Gu, J. Xiao, J. G. Zhang and C. M. Wang, Intragranular cracking as a critical barrier for high-voltage usage of layer-structured cathode for lithium-ion batteries, *Nat. Commun.*, 2017, **8**, 14101.

19 Q. Huang, L. Ma, A. Liu, X. Ma, J. Li, J. Wang and J. R. Dahn, The reactivity of charged positive $Li_{1-n}[Ni_xMn_yCo_z]O_2$ electrodes with electrolyte at elevated temperatures using accelerating rate calorimetry, *J. Power Sources*, 2018, **390**, 78–86.

20 S. Fang, D. Jackson, M. L. Dreibelbis, T. F. Kuech and R. J. Hamers, Anode-originated SEI migration contributes to formation of cathode-electrolyte interphase layer, *J. Power Sources*, 2018, **373**, 184–192.

21 J. Li, L. E. Downie, L. Ma, W. D. Qiu and J. R. Dahn, Study of the Failure Mechanisms of $LiNi_{0.8}Mn_{0.1}Co_{0.1}O_2$ Cathode Material for Lithium Ion Batteries, *J. Electrochem. Soc.*, 2015, **162**(7), A1401–A1408.

22 J. A. Gilbert, I. A. Shkrob and D. P. Abraham, Transition Metal Dissolution, Ion Migration, Electrocatalytic Reduction and Capacity Loss in Lithium-Ion Full Cells, *J. Electrochem. Soc.*, 2017, **164**(2), A389–A399.

23 J. Wandt, A. Freiberg, R. Thomas, Y. Gorlin, A. Siebel, R. Jung, H. A. Gasteiger and M. Tromp, Transition metal dissolution and deposition in Li-ion batteries investigated by operando X-ray absorption spectroscopy, *J. Mater. Chem. A*, 2016, **4**(47), 18300–18305.

24 H. Zheng, Q. Sun, G. Liu, X. Song and V. S. Battaglia, Correlation between dissolution behavior and electrochemical cycling performance for $LiNi_1/3Co_1/3Mn_1/3O_2$-based cells, *J. Power Sources*, 2012, **207**, 134–140.

25 T. Schwieters, M. Evertz, A. Fengler, M. Börner, T. Dagger, Y. Stenzel, P. Harte, M. Winter and S. Nowak, Visualizing elemental deposition patterns on carbonaceous anodes from lithium ion batteries: a laser ablation-inductively coupled plasma-mass spectrometry study on factors influencing the deposition of lithium, nickel, manganese and cobalt after dissolution and migration from the $Li_1[Ni_{1/3}Mn_{1/3}Co_{1/3}]O_2$ and $LiMn_{1.5}Ni_{0.5}O_4$ cathode, *J. Power Sources*, 2018, **380**, 194–201.

26 J. C. Garcia, J. Bareno, J. H. Yan, G. Y. Chen, A. Hauser, J. R. Croy and H. Iddir, Surface Structure, Morphology, and Stability of $Li(Ni_{1/3}Mn_{1/3}Co_{1/3})O_2$ Cathode Material, *J. Phys. Chem. C*, 2017, **121**(15), 8290–8299.

27 D. Kramer and G. Ceder, Tailoring the Morphology of $LiCoO_2$: A First Principles Study, *Chem. Mater.*, 2009, **21**(16), 3799–3809.

28 E. Cho, S.-W. Seo and K. Min, Theoretical Prediction of Surface Stability and Morphology of $LiNiO_2$ Cathode for Li Ion Batteries, *ACS Appl. Mater. Interfaces*, 2017, **9**(38), 33257–33266.

29 C. Liang, R. C. Longo, F. Kong, C. Zhang, Y. Nie, Y. Zheng and K. Cho, *Ab initio* Study on Surface Segregation and Anisotropy of Ni-rich $LiNi_{1-2y}Co_yMn_yO_2$ (NCM) ($y \leq 0.1$) Cathodes, *ACS Appl. Mater. Interfaces*, 2018, **10**(7), 6673–6680.

30 S. Sharifi-Asl, F. A. Soto, A. M. Nie, Y. F. Yuan, H. Asayesh-Ardakani, T. Foroozan, V. Yurkiv, B. Song, F. Mashayek, R. F. Klie, K. Amine, J. Lu, P. B. Balbuena and R. Shahbazian-Yassar, Facet-Dependent Thermal Instability in $LiCoO_2$, *Nano Lett.*, 2017, **17**(4), 2165–2171.

31 P. F. Yan, J. M. Zheng, J. X. Zheng, Z. G. Wang, G. F. Teng, S. Kuppan, J. Xiao, G. Y. Chen, F. Pan, J. G. Zhang and C. M. Wang, Ni and Co Segregations on Selective Surface Facets and Rational Design of Layered Lithium Transition-

Metal Oxide Cathodes, *Adv. Energy Mater.*, 2016, **6**(9), 1502455.

32 H. L. Zhang, F. Omenya, P. F. Yan, L. L. Luo, M. S. Whittingham, C. M. Wang and G. W. Zhou, Rock-Salt Growth-Induced (003) Cracking in a Layered Positive Electrode for Li-Ion Batteries, *ACS Energy Lett.*, 2017, **2**(11), 2607–2615.

33 G. Y. Chen, B. Hai, A. K. Shukla and H. Duncan, Impact of Initial Li Content on Kinetics and Stabilities of Layered $Li_{1+x}(Ni_{0.33}Mn_{0.33}Co_{0.33})(1-x)O_2$, *J. Electrochem. Soc.*, 2012, **159**(9), A1543–A1550.

34 F. Wang, S. Xiao, Z. Chang, Y. Yang and Y. Wu, Nanoporous $LiNi_{1/3}Co_{1/3}Mn_{1/3}O_2$ as an ultra-fast charge cathode material for aqueous rechargeable lithium batteries, *Chem. Commun.*, 2013, **49**(80), 9209–9211.

35 Z.-D. Huang, X.-M. Liu, S.-W. Oh, B. Zhang, P.-C. Ma and J.-K. Kim, Microscopically porous, interconnected single crystal $LiNi_{1/3}Co_{1/3}Mn_{1/3}O_2$ cathode material for Lithium ion batteries, *J. Mater. Chem.*, 2011, **21**(29), 10777–10784.

36 J. Choi and A. Manthiram, Crystal chemistry and electrochemical characterization of layered $LiNi_{0.5-y}Co_{0.5-y}Mn_{2y}O_2$ and $LiCo_{0.5-y}Mn_{0.5-y}Ni_{2y}O_2$ ($0 \leq 2y \leq 1$) cathodes, *J. Power Sources*, 2006, **162**(1), 667–672.

37 K.-S. Lee, S.-T. Myung, K. Amine, H. Yashiro and Y.-K. Sun, Structural and Electrochemical Properties of Layered $Li[Ni_{1-2x}Co_xMn_x]O_2$ ($x = 0.1 - 0.3$) Positive Electrode Materials for Li-Ion Batteries, *J. Electrochem. Soc.*, 2007, **154**(10), A971–A977.

38 J. Xiao, N. A. Chernova and M. S. Whittingham, Influence of Manganese Content on the Performance of $LiNi_{0.9-y}Mn_yCo_{0.1}O_2$ ($0.45 \leq y \leq 0.60$) as a Cathode Material for Li-Ion Batteries, *Chem. Mater.*, 2010, **22**(3), 1180–1185.

39 K. Min, K. Kim, C. Jung, S.-W. Seo, Y. Y. Song, H. S. Lee, J. Shin and E. Cho, A comparative study of structural changes in lithium nickel cobalt manganese oxide as a function of Ni content during delithiation process, *J. Power Sources*, 2016, **315**, 111–119.

40 H. Sun and K. Zhao, Electronic Structure and Comparative Properties of $LiNi_xMn_yCo_zO_2$ Cathode Materials, *J. Phys. Chem. C*, 2017, **121**(11), 6002–6010.

41 C. S. Yoon, K.-J. Park, U.-H. Kim, K. H. Kang, H.-H. Ryu and Y.-K. Sun, High-Energy Ni-Rich $Li[Ni_xCo_yMn_{1-x-y}]O_2$ Cathodes *via* Compositional Partitioning for Next-Generation Electric Vehicles, *Chem. Mater.*, 2017, **29**(24), 10436–10445.

42 S. Kuppan, A. K. Shukla, D. Membreno, D. Nordlund and G. Chen, Revealing Anisotropic Spinel Formation on Pristine Li- and Mn-Rich Layered Oxide Surface and Its Impact on Cathode Performance, *Adv. Energy Mater.*, 2017, **7**(11), 1602010.

43 F. Lin, D. Nordlund, I. M. Markus, T.-C. Weng, H. L. Xin and M. M. Doeff, Profiling the nanoscale gradient in stoichiometric layered cathode particles for lithium-ion batteries, *Energy Environ. Sci.*, 2014, **7**(9), 3077–3085.

44 C. Tian, D. Nordlund, H. L. Xin, Y. Xu, Y. Liu, D. Sokaras, F. Lin and M. M. Doeff, Depth-Dependent Redox Behavior of $LiNi_{0.6}Mn_{0.2}Co_{0.2}O_2$, *J. Electrochem. Soc.*, 2018, **165**(3), A696–A704.

45 X. Liu, D. Wang, G. Liu, V. Srinivasan, Z. Liu, Z. Hussain and W. Yang, Distinct charge dynamics in battery electrodes revealed by *in situ* and operando soft X-ray spectroscopy, *Nat. Commun.*, 2013, **4**, 2568.

46 R. Weber, C. R. Fell, J. R. Dahn and S. Hy, Operando X-ray Diffraction Study of Polycrystalline and Single-Crystal $Li_xNi_{0.5}Mn_{0.3}Co_{0.2}O_2$, *J. Electrochem. Soc.*, 2017, **164**(13), A2992–A2999.

